Ab initio phonon self-energies and fluctuation diagnostics of phonon anomalies: Lattice instabilities from Dirac pseudospin physics in transition metal dichalcogenides

Jan Berges [1,2], Erik G. C. P. van Loon [1,2], Arne Schobert [1,2], Malte Rösner [3], and Tim O. Wehling [1,2]

[1]*Institut für Theoretische Physik, Universität Bremen, Otto-Hahn-Allee 1, D-28359 Bremen, Germany*

[2]*Bremen Center for Computational Materials Science, Universität Bremen, Am Fallturm 1a, D-28359 Bremen, Germany*

[3]*Institute for Molecules and Materials, Radboud University, Heyendaalseweg 135, NL-6525 AJ Nijmegen, The Netherlands*

We present an *ab initio* approach for the calculation of phonon self-energies and their fluctuation diagnostics, which allows us to identify the electronic processes behind phonon anomalies. Application to the transition-metal-dichalcogenide monolayer 1H-TaS$_2$ reveals that coupling between the longitudinal-acoustic phonons and the electrons from an isolated low-energy metallic band is entirely responsible for phonon anomalies such as the mode softening and associated charge-density waves observed in this material. Our analysis allows us to distinguish between different mode-softening mechanisms including matrix-element effects, Fermi-surface nesting, and Van Hove scenarios. We find that matrix-element effects originating from a peculiar type of Dirac pseudospin textures control the charge-density-wave physics in 1H-TaS$_2$ and similar transition metal dichalcogenides.

I. INTRODUCTION

Different states of electronic quantum matter are often tightly linked to lattice degrees of freedom. Examples include superconductivity, periodic lattice distortions and charge-density waves (CDWs), metal-insulator transitions, and nematic, magnetic, "stripe," or excitonic order across vastly different material classes ranging from cuprate [1–5] and Fe-based high-temperature superconductors [6–8] to hydride compounds [9–11]. Disentangling the interplay of lattice and electronic degrees of freedom has remained a formidable challenge in many cases.

Phonon anomalies and mode softening are often an indicator of instabilities of the electronic system. However, the question of whether and which electronic processes are responsible for a given phonon anomaly is the source of many controversies in the literature. Often suggestions for very different mechanisms such as matrix-element effects [12], Fermi-surface nesting [13], or Van Hove scenarios [14] are made for a phonon anomaly in one and the same material [15–17]. Unambiguously distinguishing between such mechanisms is complicated and has typically required the combination of experimental probes of lattice and electron dynamics [18,19] with theoretical modeling [20].

Here, we present *ab initio* calculations of phonon self-energies, and we introduce the concept of fluctuation diagnostics [21,22] to the domain of lattice dynamics. This scheme can distinguish between different strong- and weak-coupling effects and combinations thereof in the context of phonon anomalies in a quantitative and material-specific way.

One prototypical class of materials hosting phonon anomalies are the hexagonal polytypes of the layered group-V transition metal dichalcogenides (TMDCs) [23]. Bulk and

monolayer [Fig. 1(a)] are denoted by 2H- and 1H-MX_2, where M stands for Nb or Ta and X for S or Se. Temperature-dependent phonon-mode softening and CDWs are ubiquitous in these materials, but explanations have remained controversial for several decades, and suggestions include strong-coupling arguments based on matrix elements [12,24–37] or local chemical bonding [38–43] as well as weak-coupling arguments based on Fermi-surface nesting [13,44–49] or Van Hove scenarios [14,50,51]. Our phonon-self-energy calculations and fluctuation diagnostics for monolayer 1H-TaS$_2$ reveal that coupling between the longitudinal-acoustic (LA) phonons and the electrons from an isolated low-energy metallic band [Figs. 1(b) and 1(c)] is entirely responsible for the mode softening and associated CDWs observed in this material. A combination of imperfect Fermiology conditions and matrix-element effects resulting from Dirac pseudospin textures is pinpointed as the cause of the CDW phase diagram of 1H-TaS$_2$ and similar TMDCs.

II. BARE AND SCREENED PHONONS

A general Hamiltonian describing systems of interacting electrons and phonons reads

$$H = H_{el} + H_{el\text{-}el} + H_{ph} + H_{el\text{-}ph} \tag{1a}$$

and contains one-body electron terms H_{el}, the Coulomb interaction $H_{el\text{-}el}$, pure phonon terms H_{ph}, and the electron-phonon interaction $H_{el\text{-}ph}$. The necessity to account simultaneously for the complexity of the single-particle electronic wave functions and the difficulties arising from the interactions present in H render realistic descriptions of solid-state systems notoriously complicated. One way to proceed and to gain insights in practice is via material-realistic low-energy Hamiltonians,
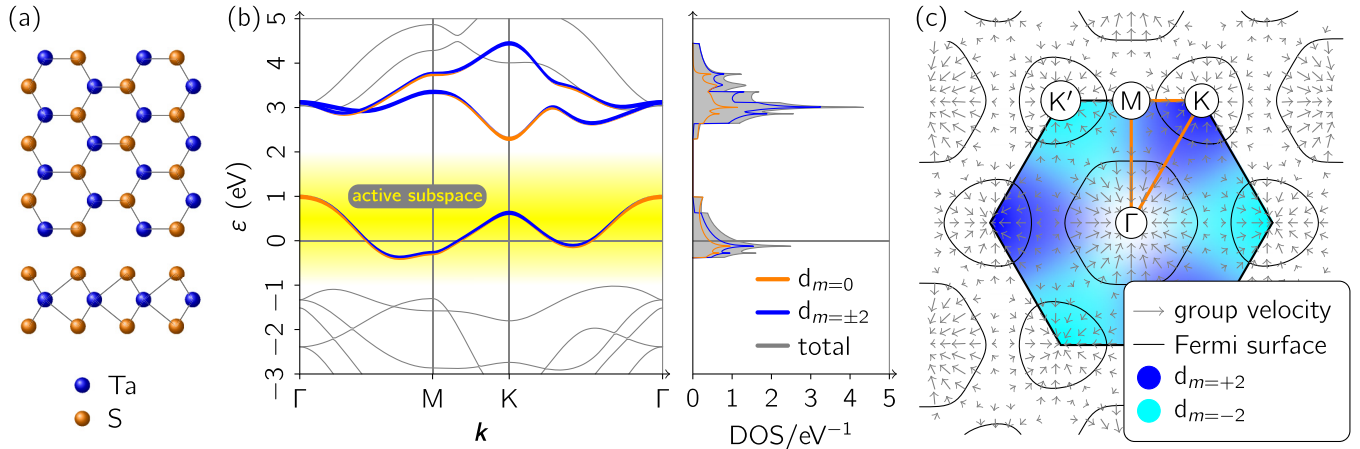
FIG. 1. Crystal and electronic structure of 1H-TaS$_2$. (a) Top and side view of the crystal structure. (b) Orbitally resolved band structure and density of states. The active subspace with the isolated low-energy metallic band is highlighted in yellow. (c) Fermi surface, orbital character, and group velocity of the low-energy band.

where the electronic degrees of freedom accounted for in H are restricted to some low-energy subspace, often also dubbed correlated subspace, target subspace, or active subspace. We will adopt the latter nomenclature. In the presented case of 1H-TaS$_2$, we take as a natural choice for the active subspace the electronic states of the low-energy band highlighted in Fig. 1(b), where spin-orbit coupling is disregarded for simplicity. A discussion of spin-orbit-coupling effects is given in Appendix D.

Then, all quantities entering H have to be partially renormalized to account for the elimination of the higher-energy degrees of freedom [52,53]. More precisely, the phonon energies entering

$$H_{\mathrm{ph}} = \sum_{\boldsymbol{q}\nu} \omega_{\boldsymbol{q}\nu} b^{\dagger}_{\boldsymbol{q}\nu} b_{\boldsymbol{q}\nu} \qquad (1\mathrm{b})$$

and the electron-phonon couplings in

$$H_{\mathrm{el\text{-}ph}} = \sum_{\boldsymbol{q}\nu\boldsymbol{k}mn} g_{\boldsymbol{q}\nu\boldsymbol{k}mn} [b^{\dagger}_{-\boldsymbol{q}\nu} + b_{\boldsymbol{q}\nu}] c^{\dagger}_{\boldsymbol{k}+\boldsymbol{q}m} c_{\boldsymbol{k}n} \qquad (1\mathrm{c})$$

are partially renormalized from the viewpoint of a full first-principles Hamiltonian and "bare" from the viewpoint of the model.

Directly experimentally observable are the fully renormalized quantities, which can be obtained by either solving the model Hamiltonian H [Eqs. (1)] or by direct treatment of the full system from first principles. For instance, density-functional perturbation theory (DFPT) [54] yields the (in practice approximate) fully renormalized phonon dispersions and electron-phonon couplings from first principles.

Partially screened phonon dispersions and electron-phonon couplings can be obtained from the constrained density-functional perturbation theory (cDFPT) [53]. Analogously to the constrained random-phase approximation (cRPA) [52] to partially screened Coulomb interactions, cDFPT excludes polarization processes taking place inside the active subspace from the screening of phonon dispersions and electron-phonon couplings. In the following, we distinguish fully from partially screened quantities by a tilde ($\sim$) on top of symbols

for the former, and we refer to them as "screened" and "bare" for brevity.

Selected bare (cDFPT) and screened (DFPT) phonon dispersions are shown in Fig. 2(a). The bare phonon dispersion of 1H-TaS$_2$ (middle), which excludes screening intrinsic to the active subspace, is smooth in reciprocal space indicating correspondingly short-range force constants, and it does not show any Kohn anomalies [55] or dynamical lattice instabilities. In contrast, the screened phonon dispersion of 1H-TaS$_2$ (left) shows strong Kohn anomalies, softening, and instabilities in the LA phonon branch in extended regions of the Brillouin zone (BZ). The instability regions include the wave vector $\boldsymbol{q} = 2/3\,\mathrm{M}$ associated with the 3×3 CDW observed in bulk [24,50,56–60] and thin 1H-TaS$_2$ [61,62]. The leading instability in the screened dispersion as signaled by the (in absolute value) largest imaginary phonon energy is indeed close to $\boldsymbol{q} = 2/3\,\mathrm{M}$. As the bare phononic system is dynamically stable and has a smooth LA dispersion in contrast to the screened one, renormalization processes taking place inside the low-energy band must be fully responsible for the mode softening and the CDW physics observed in 1H-TaS$_2$.

While the bare phonon dispersion is not directly experimentally observable, screening due to the low-energy band can be suppressed also in experiment, for instance by effective doping. If the low-energy band is completely filled, no intraband screening processes are possible. Such a situation is realized in group-VI TMDCs such as 1H-WS$_2$, which is isostructural to the undistorted high-temperature phase of 1H-TaS$_2$ and has one additional electron per primitive cell but otherwise a similar electronic band structure. As seen in Fig. 2(a), the screened phonon dispersion of 1H-WS$_2$ (right) is indeed very similar to the bare phonon dispersion of 1H-TaS$_2$ (middle). Thus, studies of isostructural compounds with different filling of the electronic bands present a route toward experimental estimates of bare phonon dispersions.

III. AB INITIO PHONON SELF-ENERGIES

There are two different ways to calculate screened phonon dispersions: first, with DFPT, and second, by approximately
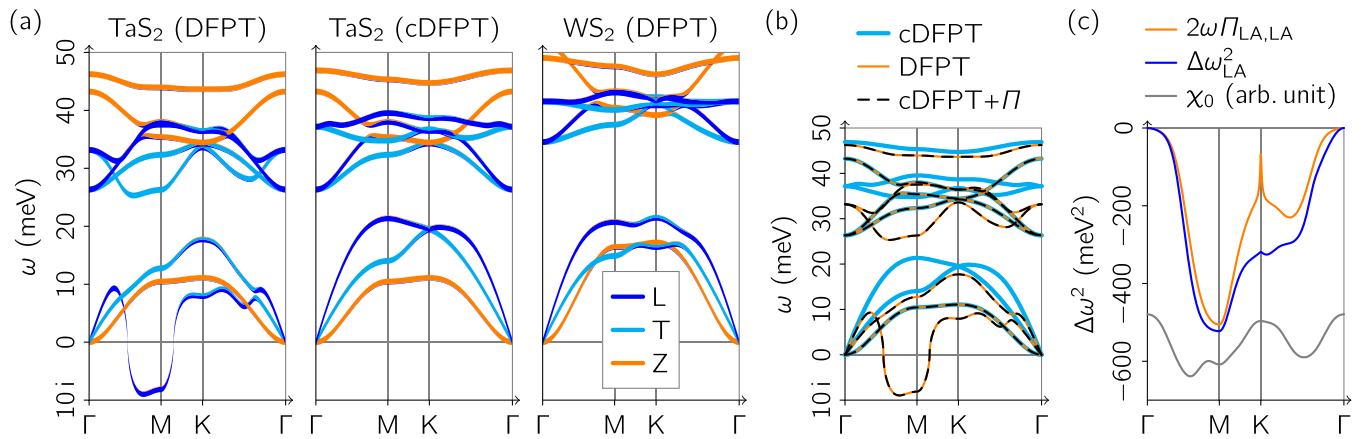
FIG. 2. (a) Phonon dispersions of 1H-TaS$_2$ (DFPT, cDFPT) and 1H-WS$_2$ (DFPT). (b) Bare phonon dispersion of 1H-TaS$_2$ from cDFPT compared to screened ones from DFPT and according to Eqs. (2) (cDFPT phonon energies renormalized *a posteriori* with the adiabatic phonon self-energy). The two screened dispersions are identical, showing that Eqs. (2) provide the exact link between cDFPT and DFPT. (c) LA diagonal matrix element of the phonon self-energy, squared-energy change of the (predominantly) LA phonon band, and bare electronic susceptibility of 1H-TaS$_2$.

solving the model Hamiltonian H. In the latter case, the experimentally observable lattice dynamics is encoded in the screened phonon Green function.

In the adiabatic approximation, the changes in phonon normal modes and energies induced by electron-phonon coupling can be obtained from the renormalized dynamical matrix

$$\widetilde{\omega}^2_{q\mu\nu} = \omega^2_{qv}\delta_{\mu\nu} + 2\sqrt{\omega_{q\mu}\omega_{qv}}\Pi_{q\mu\nu}, \qquad (2a)$$

which follows from the bare dynamical matrix $\omega^2_{qv}\delta_{\mu\nu}$, here written in its eigenbasis labeled by μ and ν, and a correction determined by the phonon self-energy

$$\Pi_{q\mu\nu} = \frac{2}{N}\sum_{kmn} g^*_{q\mu kmn}\frac{f(\varepsilon_{k+qm}) - f(\varepsilon_{kn})}{\varepsilon_{k+qm} - \varepsilon_{kn}}\widetilde{g}_{qvkmn}. \qquad (2b)$$

Here, ε and f are electronic band energies and occupations, m and n label the electronic bands that constitute our active subspace, the factor of 2 comes from the spin degeneracy, and N is the number of k points summed over. The electron-phonon coupling g appears in both bare and screened form and reads [63]

$$\overset{(\sim)}{g}_{qvkmn} = \frac{1}{\sqrt{2\omega_{qv}}}\sum_i e_{qiv}\frac{1}{\sqrt{M_i}}\langle k+qm|\frac{\overset{(}{\partial V}{}^{)}}{\partial u_{qi}}|kn\rangle, \qquad (2c)$$

where the combined index i runs over the three Cartesian displacement directions of each atom, e is an eigenvector of the bare dynamical matrix, M is the atomic mass, and ∂V is the change of the self-consistent Kohn-Sham potential upon an atomic displacement ∂u. For detailed information on Eqs. (2), we refer to Ref. [64], in particular Sec. V A. We note that the coupling g is a complex quantity that contains *a priori* arbitrary phase factors from the electronic eigenstates at k and $k + q$. Therefore, care has to be taken that a consistent gauge is applied when obtaining g and $\widetilde{g}$ from independent cDFPT and DFPT calculations. We address this problem by fixing the gauge in a localized basis of Wannier functions, which as an additional advantage allows for the Fourier interpolation to arbitrary q and k resolutions [65].

We calculated the phonon self-energy [Eq. (2b)] for the case of 1H-TaS$_2$ and renormalized the bare phonon dispersions obtained from cDFPT accordingly [Eq. (2a)]. A comparison of the bare phonon dispersion to the screened ones as obtained from DFPT and from the phonon self-energy is shown in Fig. 2(b). We see that both screened dispersions are the same throughout the BZ path. Indeed, the approximations involved in the DFPT calculation (adiabaticity and a semilocal exchange-correlation functional) can be shown to be equivalent to Eqs. (2) [53]. Exchange-correlation effects beyond RPA only enter through the difference between g and $\widetilde{g}$.

The phonon self-energy is a matrix in the space of atomic displacement coordinates. The renormalization according to Eqs. (2) accounts for this full matrix structure. To lowest order, corrections to the bare phonon energies from low-energy electronic screening are contained in the diagonal components Π_{qvv} of the phonon self-energy. Figure 2(c) shows a comparison of the change $\Delta\omega^2_{LA} = \widetilde{\omega}^2_{LA} - \omega^2_{LA}$ of the (predominantly) LA phonon band upon low-energy electronic screening to the corresponding diagonal matrix element $2\omega\Pi_{LA,LA}$ in the eigenbasis of the bare phonons. We see that $\Delta\omega^2_{LA}$ and $2\omega\Pi_{LA,LA}$ show a qualitatively similar q dependence, but there are also deviations between the two, particularly close to the K point. This is due to changes in the normal-mode eigenvectors upon renormalization. Thus, the diagonal part of the phonon self-energy can serve as a qualitative guide for the understanding of phonon-renormalization phenomena, but quantitative calculations must account for its full matrix structure.

Phonon self-energies, screened, and bare phonon dispersions for 1H-TaS$_2$ have also been calculated in Ref. [66], albeit with a different procedure. While the screened phonon dispersions in Ref. [66] are similar to those depicted in Fig. 2(a), the bare phonon dispersions in Ref. [66], which have not been obtained from cDFPT but were estimated from DFPT data, differ from those found here by not being smooth but still displaying a dip at the wave vector associated with the 3×3 CDW. Possible origins of this discrepancy are that the analysis in Ref. [66] has been restricted to the diagonal components

of the phonon self-energy and that the calculations involved only screened electron-phonon vertices instead of the required combination of bare and screened vertices as in Eq. (2b).

Several works, e.g., Refs. [12,33,40,41,67,68], addressed the renormalization of phonons due to chosen subsets of interaction processes, but they had to rely on further, often semiempirical models or assumptions on the shape of the "bare" phonon dispersion. In this context, partially screened phonons and electron-phonon couplings from cDFPT as considered in this work are very helpful, since cDFPT delivers an unambiguous bare starting point. Additionally, when analyzing nonadiabaticity [69–75], cDFPT can provide a well-defined adiabatic starting point together with the correct coupling for nonadiabatic correction terms.

IV. FLUCTUATION DIAGNOSTICS OF PHONON SELF-ENERGIES

We seek to understand unambiguously how the electrons renormalize the phonon dispersion. The expression for the phonon self-energy makes this possible: Each summand in Eq. (2b) quantifies how much specific electronic states contribute to the phonon self-energy and allows us to identify the mechanism responsible for the phonon renormalization. A similar kind of "fluctuation diagnostics" has previously been applied in correlated electron systems to identify antiferromagnetic correlations as the mechanism responsible for the pseudogap in the Hubbard model [21].

The phonon self-energy as approximated by Eq. (2b) is a BZ, band, and spin sum of electronic fluctuations

$$\chi^0_{qkmn} = \frac{f(\varepsilon_{k+qm}) - f(\varepsilon_{kn})}{\varepsilon_{k+qm} - \varepsilon_{kn}} \quad (3a)$$

weighted by the coupling matrix elements, for which we now adopt a symmetrized, Hermitian representation [76],

$$g^2_{q\mu\nu kmn} = \frac{g^*_{q\mu kmn} \cdot \widetilde{g}_{q\nu kmn} + \widetilde{g}^*_{q\mu kmn} \cdot g_{q\nu kmn}}{2}. \quad (3b)$$

By analyzing

$$\Pi_{q\mu\nu kmn} = g^2_{q\mu\nu kmn} \cdot \chi^0_{qkmn} \quad (3c)$$

as a function of electronic momenta k and $k + q$, we can perform "fluctuation diagnostics" and identify which fermionic fluctuations contribute most dominantly to the phonon self-energy. Furthermore, by comparison of Π to χ_0 and g^2 we can directly distinguish purely electronic band-structure and "Fermiology" effects from matrix-element effects.

One can similarly quantify the contribution of electronic states from a certain energy range to the phonon renormalization. Considering a single band for brevity,

$$\Pi(\Delta) = \frac{2}{A} \int d^2k \, \Pi_k \, \Theta(|\varepsilon_k| - \Delta) \, \Theta(|\varepsilon_{k+q}| - \Delta) \quad (4a)$$

with the BZ area A accounts only for fermionic modes with energies outside of an energy window $[-\Delta, +\Delta]$ around the Fermi level. In the renormalization-group spirit, this corresponds to integrating out all electrons outside of the energy window. The full result of the calculation is recovered by

letting $\Delta \to 0$. The derivative

$$\partial_\Delta \Pi(\Delta) = -\frac{2}{A} \int d^2k \, \Pi_k \, [\delta(|\varepsilon_k| - \Delta) \, \Theta(|\varepsilon_{k+q}| - \Delta)$$
$$+ \Theta(|\varepsilon_k| - \Delta) \, \delta(|\varepsilon_{k+q}| - \Delta)] \quad (4b)$$

then quantifies the contributions of electronic states with energies from the shell $|\varepsilon_k| = \Delta$ to Π [77].

Matrix-element effects, Fermi-surface nesting, and Van Hove scenarios as possible causes of phonon-mode softening manifest markedly differently in the fluctuation diagnostics. For a generic d-dimensional system, in the absence of any Fermi-surface anomalies like nesting, $\Pi(\Delta)$ remains finite as $\Delta \to 0$. On the other hand, Fermi-surface nesting, as realized in one-dimensional systems for $q_c = 2k_F$ [78] or also in higher-dimensional systems for parallel sheets of the Fermi surface linked by some nesting vector q_c, leads to diverging $\Pi_{q_c}(\Delta) \sim \ln|\Delta|$ and $\partial_\Delta \Pi_{q_c}(\Delta) \sim 1/\Delta$ [79]. We expect the same kind of divergences in so-called Van Hove scenarios, where the Fermi level is at the energy of Van Hove singularities (VHS) in the electronic density of states, e.g., for wave vectors $q_c = q_{VHS}$ connecting two saddle points [14] as found in 1H-TaS$_2$. In turn, nesting and Van Hove scenarios can be clearly distinguished in k-space fluctuation diagnostics by dominant contributions to Π originating from line segments in the case of nesting and being centered around the Van Hove points in the latter case. The role of the matrix elements is seen by comparing χ_0 to Π.

V. FLUCTUATION DIAGNOSTICS OF LA-PHONON-MODE SOFTENING AND CDW FORMATION IN 1H-TaS$_2$

The CDW physics of 1H-TaS$_2$ is associated with softening of LA phonon modes in the undistorted phase toward dynamical lattice instabilities. As shown in Sec. II, this softening is entirely due to coupling of the phonons to the electrons from the active subspace in Fig. 1(b). In the following, we identify which processes inside this active subspace contribute most dominantly to the phonon-mode softening for pristine (Sec. V A) and doped 1H-TaS$_2$ (Sec. V B). Only the LA diagonal elements of $2\omega g^2$ and $2\omega\Pi$ in the eigenbasis of the bare phonons are shown. The prefactor of 2ω cancels with the prefactor in Eq. (2c). Most subscripts are omitted for brevity. All computational parameters are listed in Appendix C.

A. Pristine 1H-TaS$_2$

The wave vector associated with the 3×3 CDW in pristine 1H-TaS$_2$, i.e., at the chemical potential $\mu = 0$, is $q = 2/3$ M. The fluctuation diagnostics of the corresponding phonon self-energy $2\omega\Pi$ [Fig. 3(a)] reveals that the dominant contributions to $2\omega\Pi$ are peaked in distinct regions of k space: The Fermi surface (contour) of undoped 1H-TaS$_2$ consists of three hole pockets encircling Γ, K, and K′, respectively. The strongest contributions to $2\omega\Pi$ originate from regions where the original pocket around K approximately touches the pocket around K′, shifted by $-q$, and vice versa. There are two such regions of touching K and K′ pockets (intervalley processes) and two regions of touching K and shifted K pockets or touching K′ and shifted K′ pockets (intravalley processes) in the BZ. While all four of these regions contribute
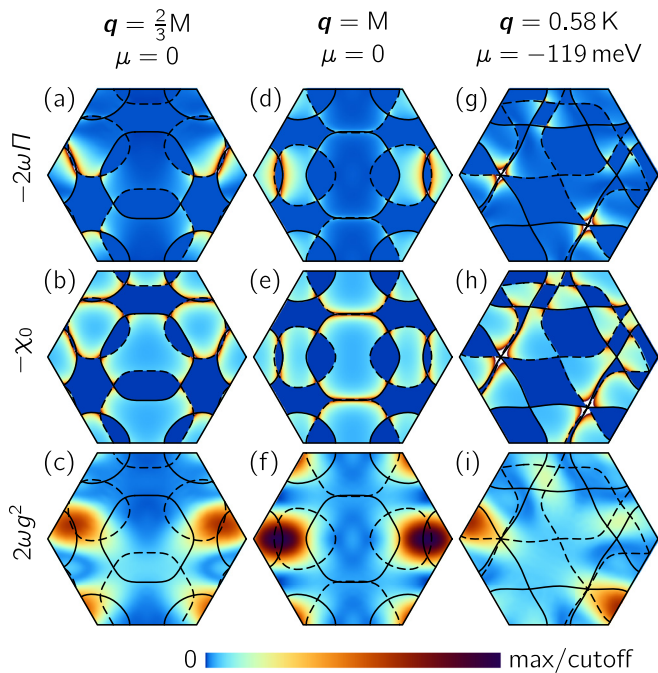
FIG. 3. Momentum-resolved fluctuation diagnostics of LA-phonon-mode softening at $q = 2/3$ M (left) and $q = $ M (middle) in undoped 1H-TaS$_2$ as well as at $q = 0.58$ K (right) at Van Hove filling (chemical potential $\mu = -119$ meV). The k-dependent contributions to the phonon self-energy $2\omega\Pi$, the bare electronic susceptibility χ_0, and the coupling matrix elements $2\omega g^2$ are shown color-coded. Solid (dashed) lines indicate the Fermi surface (shifted by the respective q vectors).

to the bare electronic susceptibility χ_0 [Fig. 3(b)], only the two regions associated with the intervalley coupling contribute significantly to the phonon self-energy $2\omega\Pi$ [Fig. 3(a)]. The coupling matrix elements $2\omega g^2$ [Fig. 3(c)] filter out these two of the four regions of (approximately) touching hole pockets.

One might be tempted to explain the contributions to $2\omega\Pi$ from the two remaining regions with touching K and K$'$ pockets in terms of nesting. However, our results rule out such a nesting scenario: As a first indication already seen in Fig. 2(c), q dependencies in χ_0 are much less pronounced than those in $2\omega\Pi$, which is opposite to the expectation of a logarithmically divergent χ_0 in a nesting scenario. $2\omega\Pi$ shows a pronounced extremum for $q = $ M, while χ_0 shows significantly smaller and opposite variations. The k-resolved fluctuation diagnostics of $2\omega\Pi$ at $q = $ M [Fig. 3(d)] shows that dominant contributions come again from K and K$'$ pockets, which are now slightly overlapping rather than approximately touching and clearly not nested at $q = $ M. Indeed, there is nesting for the hole pocket around Γ which contributes to χ_0 [Fig. 3(e)]. However, the resultant approximate divergence is logarithmic, thus already weak on the level of χ_0, and fully masked by matrix-element effects in the phonon self-energy. Consequently, matrix-element effects clearly dominate here.

A basic and widely used model [33,80] of the interaction between electrons and LA phonons assumes that $g_{qk} \sim (v_k - v_{k+q}) \cdot q$, which suggests that coupling is most effective if the group velocities $v_k = \nabla_k \varepsilon_k$ and v_{k+q} of the coupled electronic states are opposed to each other and parallel to q. Interestingly,

those regions with strong (suppressed) electron-phonon coupling identified by our analysis [Figs. 3(c), 3(f), and 3(i)] are characterized by group velocities mainly orthogonal (parallel) to the phonon momentum q, which is exactly opposite to the expectation from the model. The reason for this deviation is the massive-Dirac-fermion nature of the low-energy-band states and associated pseudospin textures, as will be explained in Sec. VI B.

B. Doping dependence and Van Hove scenarios

Charge doping is known to affect CDW instabilities by shifting the ordering wave vectors and suppressing or supporting CDW order in many materials from high-T_c superconductors [4] to TMDCs [44,81–84] and 1H-TaS$_2$ in particular [62,66,85,86]. We studied the dependence of the LA phonon mode on charge doping in the phonon-self-energy formalism [Eqs. (2)] by changing the electronic chemical potential μ in the model Hamiltonian H. In doing so, we disregard changes in the screened coupling $\widetilde{g}$. This approximation is justified by the small relative difference between g and $\widetilde{g}$ in the undoped case. A comparison of phonon self-energies and resulting screened phonon dispersions for hole doping ($\mu = -119$ meV), the charge-neutral system ($\mu = 0$), and electron doping ($\mu = 91$ meV) is given in Fig. 4. In line with former theoretical results [66] and experiments [62], we find that electron doping pushes the wave vector of the leading lattice instability toward the M point. Hole doping of $\mu = -119$ meV, on the other hand, shifts the instabilities further away from M and also lets additional "fragile" instabilities between Γ and K emerge, which depend very sensitively on the thermal broadening $k_B T$ of the electronic Fermi distribution function. At smallest temperatures $k_B T \approx 1$ meV, the leading instabilities occurring in the phonon dispersions [Fig. 4(a)] coincide with the extrema of the corresponding phonon self-energies [Fig. 4(b)]. The latter are fully determined by the Fermiology conditions of touching K and K$'$ pockets and (approximately) superimposed Van Hove points over the whole range of doping levels. However, these extrema are by no means isolated points of enhanced/divergent phonon self-energies but embedded in extended q-space regions with appreciable mode softening.

Fluctuation diagnostics (Fig. 5) reveals the mechanisms behind the doping dependencies found in Fig. 4: While the filter determined by the electron-phonon coupling remains the same regardless of the doping level [blue-shaded regions in Fig. 5(a)], electron doping shrinks the hole pockets around K, K$'$, and Γ. Correspondingly, touching or partially overlapping K and K$'$ pockets are realized for CDW wave vectors larger than $q = 2/3$ M. For $\mu = 91$ meV, $q = $ M leads to touching K and K$'$ pockets. Therefore, contributions to $2\omega\Pi$ are correspondingly enhanced at M, while the mode softening at $q = 2/3$ M is weaker in this electron-doped case. Hence, nearly overlapping hole pockets and corresponding contributions to χ_0 are necessary for effective mode softening. If the instability at M in this case was a pure nesting effect, one should find a logarithmic divergence in the energy-resolved fluctuation diagnostics in $\Pi(\Delta)$ and a corresponding $1/\Delta$ divergence in $\partial_\Delta\Pi(\Delta)$. As one can see from Fig. 5(b), we do not find such divergences for the electron-doped case at $q = $ M nor
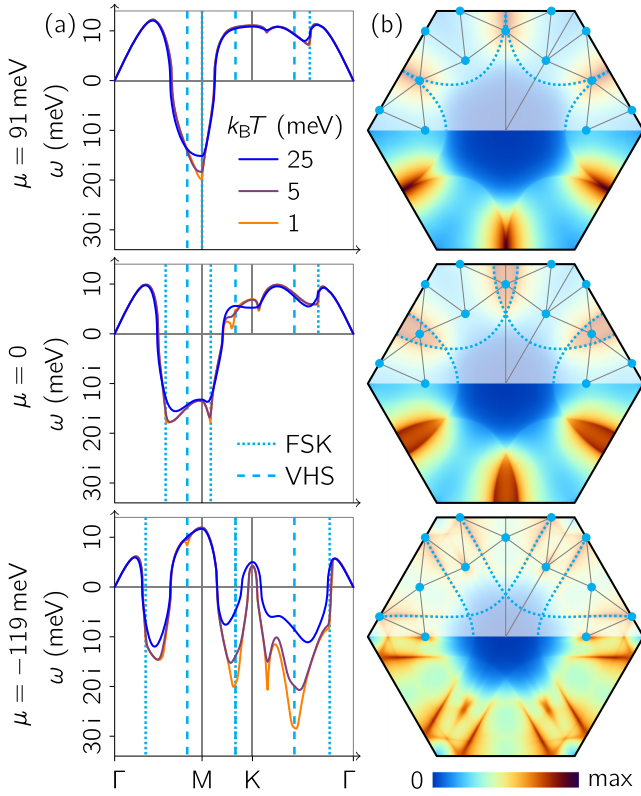
FIG. 4. (a) LA phonon dispersion and (b) q-dependent LA phonon self-energy $(-2\omega\Pi)$ at different chemical potentials μ. At $\mu = -119$ meV, the VHS is at the Fermi level; at $\mu = 0$, we have no doping; at $\mu = 91$ meV, we have touching K and K' pockets for $q = $ M. The dispersion is shown for different broadenings k_BT, the phonon self-energy only for $k_BT = 1$ meV. Special q points are marked in cyan, where FSK and VHS stands for touching K and K' pockets and superimposed saddle points, respectively.

for the undoped case at $q = 2/3$ M (cf. Appendix A). Thus, sufficiently large matrix elements of the electron-phonon coupling and sufficiently large albeit finite bare electronic susceptibilities are of central importance in both cases. This finding is in line with Refs. [87–90].

For an electronic chemical potential of $\mu = -119$ meV one realizes "Van Hove doping," i.e., hole doping such that the electronic VHS at $k = 0.58$ K and symmetry-equivalent k points are directly at the Fermi level. In this situation, it is possible to realize phonon-mode softening as put forward in the so-called Van Hove scenario [14], where low-energy electronic fluctuations from the vicinity of VHS yield diverging contributions to the bare electronic susceptibility and possibly to the phonon self-energy. However, the situation in 1H-TaS$_2$ at Van Hove doping is intricate: There are dynamical lattice instabilities in large parts of the BZ, particularly between Γ and K. For most unstable parts of the Γ-K section, one has imperfect nesting. The notable exception is $q_{VHS} = 0.58$ K, which realizes a Van Hove scenario on top of imperfect nesting. For this q vector there are sizable contributions to χ_0 from the vicinity of the VHS [Fig. 3(h)]. Also the electron-phonon matrix elements are nonzero in the vicinity of the matched VHS [Fig. 3(i)]. Thus, at sufficiently small energies, the VHS-induced logarithmic divergence in χ_0 manifests

also in $2\omega\Pi$ [Fig. 3(g)]. That becomes more obvious in the energy-resolved fluctuation diagnostics [Fig. 5(b)]: We find divergences $\partial_\Delta\Pi \sim 1/\Delta$ and $\Pi \sim \ln \Delta$ as expected in the Van Hove scenario (cf. Appendix A). However, in absolute numbers, very small energy scales have to be reached for the Van Hove contribution to dominate over more conventional effects (e.g., imperfect nesting and matrix-element effects): That can be seen from the dependence of the screened phonon dispersions on electronic broadening in the VHS-doped case [Fig. 4(a)]. q_{VHS} clearly defines the leading instability only for electronic temperatures below $k_BT \approx 1$ meV, while instabilities in large parts of the BZ exist already at $k_BT = 25$ meV.

Taken together, our fluctuation diagnostics confirms that Fermiology alone is insufficient to understand the phonon renormalization. The matrix-element filter provided by the electron-phonon coupling in its interplay with the Fermiology determines the phonon self-energies and mode softening in 1H-TaS$_2$.

VI. TIGHT-BINDING AND DIRAC MODEL OF ELECTRON-PHONON COUPLING IN 1H-TaS$_2$

To obtain a microscopic understanding of the matrix-element effects, we calculate the electron-phonon coupling for a nearest-neighbor tight-binding (TB) model, following two widely used approaches by Varma *et al.* [33,80], and we compare it to the *ab initio* results. We find that the momentum dependence of the electron-phonon coupling results from the multiorbital nature of the active subspace and can be understood in terms of pseudospin textures of massive Dirac fermions.

A. Tight binding

We consider a nearest-neighbor TB model

$$H_k^{\alpha\beta} = \varepsilon_0^{\alpha\beta} + \sum_{n=1}^{6} t_n^{\alpha\beta} e^{ia_n k} \qquad (5)$$

with the bond vectors a_n and orbital indices α and β. The on-site energy ε_0 and the hopping t_n are specified in Appendix B. As seen in Fig. 6(a), the resulting band structure fits the reference from density-functional theory (DFT) quite well, particularly the low-energy band.

In Appendix B we briefly review how to derive an approximate expression for the corresponding electron-phonon coupling [80]. Transforming Eq. (B5) into the band eigenbasis of H_k and H_{k+q} yields

$$g_{q\nu kmn} \sim \sum_l \left(A_{qk}^{ml} v_k^{ln} - v_{k+q}^{ml} A_{qk}^{ln} \right) \cdot e_{q\nu}, \qquad (6)$$

where $v_k^{mn} = \sum_{\alpha\beta}(U_k^{\alpha m})^* (\nabla_k H_k^{\alpha\beta}) U_k^{\beta n}$ is the velocity operator in the band basis and $A_{qk}^{mn} = \sum_\alpha (U_{k+q}^{\alpha m})^* U_k^{\alpha n}$ is a unitary matrix which describes the overlap of the lattice-periodic part of band state n at k with band state m at $k + q$. Here, U_k is the matrix of right eigenvectors of H_k which fulfills $\sum_{\alpha\beta}(U_k^{\alpha m})^* H_k^{\alpha\beta} U_k^{\beta n} = \varepsilon_{kn}\delta_{mn}$.

Another widely used approximation [cf. Eqs. (A.11) and (A.12) of Ref. [80] and Eq. (2) of Ref. [33]] neglects the off-diagonal matrix elements of the velocity operator in the band
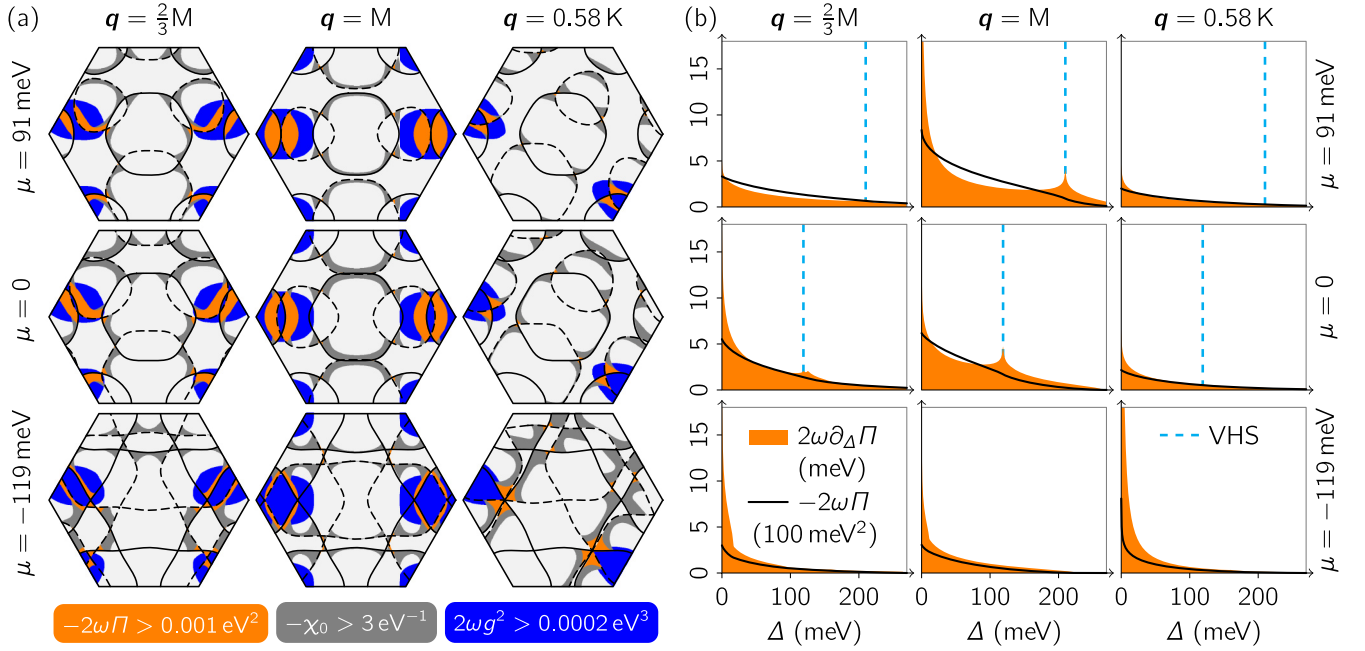
FIG. 5. (a) Momentum- (k-) and (b) energy-resolved fluctuation diagnostics of LA-phonon-mode softening in 1H-TaS$_2$ as a function of charge doping (the electronic chemical potential μ) at $q = 2/3$ M, M, and K. The blue-, gray-, and orange-shaded regions in panel (a) indicate k points with significant contributions to the phonon self-energy, the bare electronic susceptibility, and the electron-phonon coupling as defined in Eqs. (3).

basis and thus only accounts for the standard electronic group velocities $v_k^{nn} = \nabla_k \varepsilon_{nk}$,

$$g_{qvkmn} \sim A_{qk}^{mn} (v_k^{nn} - v_{k+q}^{mm}) \cdot e_{qv}. \quad (7)$$

In Figs. 6(b) and 6(c) we show the k-dependent coupling of the LA phonons with the low-energy band for $q = 2/3$ M within the approximations of Eqs. (6) and (7). According to (c)DFPT [Fig. 3(c)] there are only two spots in the vicinity of K and K' where the coupling is large. Equation (6) reproduces the structure of the coupling found in (c)DFPT qualitatively [Fig. 6(b)]. However, the simplified Eq. (7) does not capture

the relevant physics, as the resulting coupling is much weaker and has its maximum in the hole pocket around Γ [Fig. 6(c)]. Therefore, intraband variation of orbital characters and the full matrix structure of the velocity operator must be decisive in determining the electron-LA-phonon coupling.

B. Massive Dirac fermions

Both the TB model and the first-principles calculations (Sec. V A) suggest that the coupling between electrons and LA phonons is strong when the group velocities of the electronic states are (largely) orthogonal to the phonon momentum q. This is exactly opposite to the expectation from Eq. (7). To understand the origin of this behavior, we resort to an even simpler model and describe the low-energy band of 1H-TaS$_2$ around K and K' in terms of massive Dirac fermions [91]:

$$H_D = v_0(\tau p_x \sigma_x + p_y \sigma_y) + \frac{\Delta}{2}\sigma_z. \quad (8)$$

Here, $\tau = \pm 1$ is the valley index, which selects between regions around K and K' [Fig. 1(c)], v_0 is an effective velocity playing the role of the speed of light in the relativistic Dirac equation, and Δ is the band gap. The Pauli matrices σ_i with $i \in \{x, y, z\}$ act on pseudospinors $\chi_{\tau p}$ from a space of two Ta d orbitals: The upper (lower) component of $\chi_{\tau p}$ describes the d orbitals with orbital angular momentum $m = 0$ ($m = 2\tau$). The eigenvalues of H_D at momentum p relative to K or K' are $\varepsilon_p = \pm\sqrt{\Delta^2/4 + v_0^2 p^2}$, as shown in Fig. 7(a).

The velocity operator resulting from the Dirac Hamiltonian [Eq. (8)] is

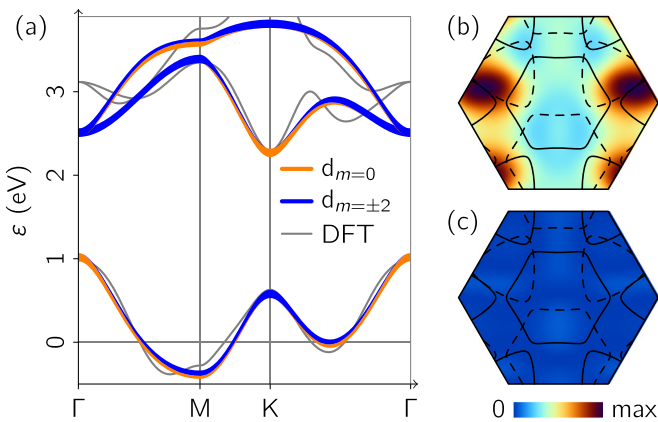$$v_D = \nabla_p H_D = v_0(\tau e_x \sigma_x + e_y \sigma_y). \quad (9)$$

FIG. 6. (a) Electronic band structure from the TB model [Eq. (5)] compared to DFT, (b) the resulting k-resolved coupling $2\omega g^2$ of LA phonons with the low-energy band for $q = 2/3$ M according to Eq. (6), and (c) the corresponding simplified coupling defined in Eq. (7).
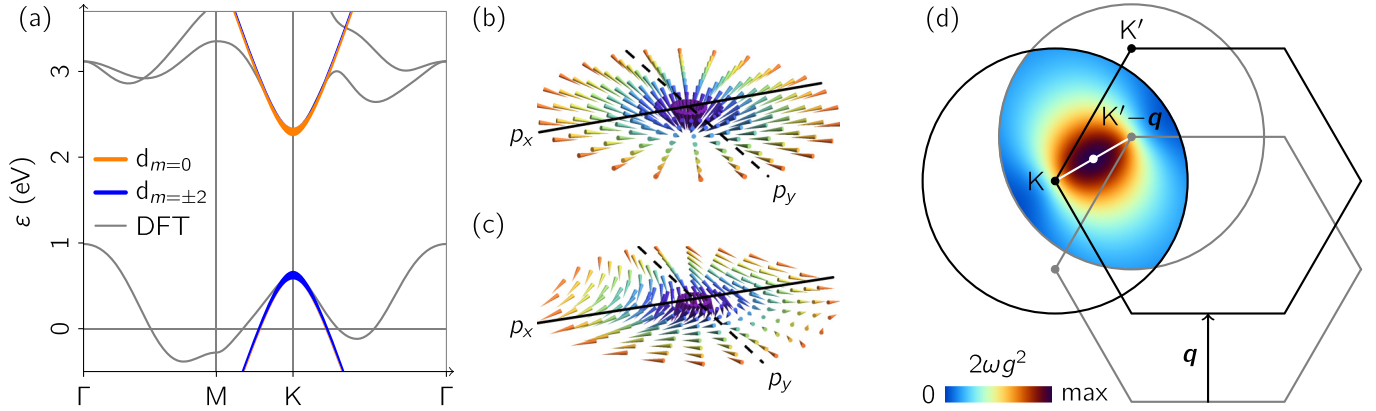
FIG. 7. (a) Electronic band structure from a model of massive Dirac fermions compared to DFT. (b, c) Dirac pseudospin texture of the lower band around (b) K and (c) K′. (d) The resulting intervalley electron-phonon coupling strength $2\omega g^2$ for $\boldsymbol{q} = 2/3$ M exhibits a clear maximum halfway between K and K′ − $\boldsymbol{q}$.

This operator describes the change in both eigenvalues *and* the change in eigenvectors of H_D. As in relativistic quantum theory, the Dirac velocity operator is independent of $\boldsymbol{k} = \mathrm{K}^{(\prime)} + \boldsymbol{p}$ inside either valley. Therefore, the intravalley electron-phonon coupling according to Eq. (6) vanishes. Thus, the massive-Dirac-fermion nature of the quasiparticles and the resultant pseudospin-momentum coupling causes the smallness of the matrix elements of the electron-phonon coupling associated with intravalley scattering, as seen in Figs. 3(c) and 6(b).

Regarding the intervalley coupling, we first note that the operator $\boldsymbol{v}_D$ has contributions perpendicular and parallel to the equal-energy contours of H_D [92], resulting from the pseudospin-momentum coupling intrinsic to the Dirac equation [Eq. (8)]. Hence, the Dirac velocity operator $\boldsymbol{v}_D$ is very different from the naive expectation for the group velocity $\boldsymbol{v}_{\boldsymbol{k}} = \nabla_{\boldsymbol{k}} \varepsilon_{\boldsymbol{k}} = v_0^2 \boldsymbol{k} / \varepsilon_{\boldsymbol{k}}$, which only describes the change in energy eigenvalues and always points perpendicular to the equal-energy contours.

The rotation of pseudospins in the lower band around K and K′ indeed gives rise to a velocity component *parallel* to the equal-energy contours. This allows, generically, for intervalley coupling between electrons and LA phonons at arbitrary angles between equal-energy contours and phonon momentum $\boldsymbol{q}$, in contrast to the simplified model of Eq. (7). For the specific analysis of intervalley scattering in TMDCs, one has to be careful since in the model of Eq. (8) the orbital character associated with one of the pseudospin components changes from $m = +2$ to -2 when going from K to K′.

Let χ_K and $\chi_{K'}$ be pseudospinors belonging to lower-band states at $\boldsymbol{k} = \mathrm{K} + \boldsymbol{p}$ and $\boldsymbol{k} + \boldsymbol{q} = \mathrm{K}' + \boldsymbol{p}'$ located in the K and K′ valleys, respectively. That is, χ_K ($\chi_{K'}$) is the negative-eigenvalue eigenvector of H_D for $\tau = +1$ (-1) and for momentum $\boldsymbol{p}$ ($\boldsymbol{p}'$). Then, the electron-phonon coupling according to Eq. (6) can be expressed using projection operators P_0 on the $m = 0$ orbitals:

$$g_{\boldsymbol{q}\boldsymbol{k}} \sim \chi_{K'}^{\dagger} \big(\boldsymbol{v}_K P_0 - P_0 \boldsymbol{v}_{K'} \big) \chi_K \cdot \boldsymbol{e}_{\boldsymbol{q}\nu}. \tag{10}$$

In the same matrix representation as used in Eq. (8) we have $P_0 = (1 + \sigma_z)/2$, where 1 is the 2×2 identity matrix. With

Eq. (9) we then find

$$g_{\boldsymbol{q}\boldsymbol{k}} \sim \chi_{K'}^{\dagger} \sigma_x \chi_K \, (\boldsymbol{e}_x + i\boldsymbol{e}_y) \cdot \boldsymbol{e}_{\boldsymbol{q}\nu}. \tag{11}$$

The direction of the phonon eigenvector $\boldsymbol{e}_{\boldsymbol{q}\nu}$ enters merely as a phase factor. For the absolute value of the LA coupling, the angle between the equal-energy contours and $\boldsymbol{q}$ is not decisive. Instead, the coupling strength is determined by $\chi_{K'}^{\dagger} \sigma_x \chi_K$ and thus results from the pseudospin textures of the lower-band states around K and K′ shown in Figs. 7(b) and 7(c) alone. Contributions to g according to Eq. (11) arise from opposite-sign pseudospin projections $\chi^{\dagger} \sigma_i \chi$ of χ_K and $\chi_{K'}$ in the y or z direction and equal-sign pseudospin projection in the x direction. The z projection of all lower-band pseudospins is "down," which does not lead to contributions to g. The winding of the in-plane pseudospin component is opposite in the K and K′ valleys [Figs. 7(b) and 7(c)]. The condition of maximum coupling $|g|$ is fulfilled if χ_K and $\chi_{K'}$ belong to time-reversed crystal momenta, $\boldsymbol{p} = -\boldsymbol{p}'$, preferably with large absolute value. This is realized for $\boldsymbol{k}$ being half-way between K and the shifted K′ point [Fig. 7(d)], i.e., exactly in the region where we find enhanced electron-phonon coupling in (c)DFPT [Fig. 3(c)] and also in the TB model [Fig. 6(b)]. Hence, the momentum-space selection rule for the electron-phonon coupling, which we identified using fluctuation diagnostics, originates from the massive-Dirac-fermion nature of the low-energy-band states in 1H-TaS$_2$.

VII. CONCLUSIONS

We have presented an *ab initio*–based scheme for the calculation of phonon self-energies from material-realistic low-energy models. This approach allows us to generalize the idea of fluctuation diagnostics [21] to electron-phonon-coupled systems and to identify the contributions of the different electronic fluctuation channels to the renormalization of phonons in complex materials.

Application of this scheme to the model CDW compound of 1H-TaS$_2$ showed that polarization processes taking place in an isolated low-energy metallic band are entirely responsible for the mode softening and CDW physics in this material. While Fermi-surface effects originating from this band can

affect the CDW ordering wave vector, we give direct proof that lattice instabilities in 1H-TaS$_2$ are largely controlled by electron-phonon-coupling matrix-element effects. The origin of these matrix-element effects is shown to be the massive-Dirac-fermion nature, the resultant pseudospin textures, and associated anomalous intervalley velocity matrix elements of electronic quasiparticles in the low-energy band of 1H-TaS$_2$. Thus, the fluctuation diagnostics provides a purely *ab initio* way to settle the long-standing debate on the nature of CDW physics in group-V TMDCs and to reveal its physical origin.

The scheme for the calculation of phonon self-energies and for performing fluctuation diagnostics outlined here should be generally insightful to disentangle the interplay of electronic and lattice degrees of freedom in complex materials. Promising areas of future application range from materials like TiSe$_2$, where excitonic physics intertwines with lattice instabilities [93–100], to strongly correlated electron systems with coupled lattice, spin, and superconducting phenomena as take place in Fe-based superconductors [6–8] or in proximity to stripe phases in cuprate high-temperature superconductors [1–5]. Finally, generalizations beyond the adiabatic limit should be conveniently possible and allow, e.g., for the description of phonons in electronic flat-band systems such as twisted bilayer graphene.

APPENDIX A: DIVERGENCE IN THE VAN HOVE SCENARIO

In Sec. V B we state that we find the expected divergences $\Pi \sim \ln \Delta$ and $\partial_\Delta \Pi \sim 1/\Delta$ of the phonon self-energy and its derivative for small energy-window sizes Δ. While from Fig. 5(b) the exact type of divergence does not become evident, the representation of the data shown Fig. 8 is more suitable for this purpose.

APPENDIX B: DETAILS OF THE TB MODEL

In the tight-binding model discussed in Sec. VI A, we only consider transitions between d orbitals localized at neighboring Ta atoms. The hopping to the nth neighbor at the relative position $\boldsymbol{a}_n = r_n(\cos \varphi_n, \sin \varphi_n)$ is

$$t_n = \left[\frac{r_n}{a}\right]^\lambda R_{\varphi_n} M^n t_0 M^n R_{-\varphi_n}, \tag{B1}$$

where $r_n = a$ and $\varphi_n = n\pi/3$ are bond length and angle, $\lambda = -5$ quantifies the distance dependence of d-d bonds [16,101], t_0 is the hopping in the x direction, M is the reflection $y \mapsto -y$, and R is a rotation about the z axis.

In the basis of complex harmonics $d_{m=0} = d_{z^2}$ and $d_{m=\pm 2} = (d_{x^2-y^2} \pm i d_{xy})/\sqrt{2}$, we have $M = \mathrm{diag}(1, \sigma_x)$ with
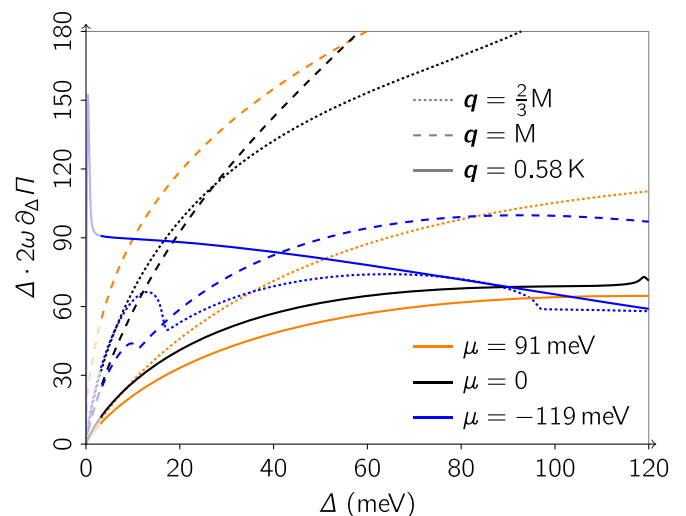

FIG. 8. Product of energy-window size Δ and derivative of phonon self-energy $\partial_\Delta \Pi$ for all situations shown in Fig. 5(b). Different line styles (dotted, dashed, solid) refer to different $\boldsymbol{q}$ points while different line colors (orange, black, blue) refer to different chemical potentials. For a diverging $\partial_\Delta \Pi \sim 1/\Delta$, the displayed quantity is a nonzero constant in the limit of small Δ. As expected, this is only the case in the Van Hove scenario (solid, blue line). The artefacts in the grayed-out region where $\Delta < 3$ meV are due to smearing-related numerical inaccuracies.

the Pauli matrix σ_x and $R_\varphi = \mathrm{diag}(1, e^{2i\varphi}, e^{-2i\varphi})$. The on-site energy and zeroth hopping read

$$\varepsilon_0 = \mathrm{diag}(\xi = 1.85, \eta = 2.30, \eta) \text{ eV},$$

$$t_0 = \begin{bmatrix} \alpha = -0.14 & \gamma = 0.34 - 0.27i & \gamma^* \\ \gamma & \beta = 0.03 + 0.31i & \delta = -0.29 \\ \gamma^* & \delta & \beta^* \end{bmatrix} \text{eV}. \tag{B2}$$

The number of independent parameters has been reduced using the point symmetries of the crystal. Their given values have been obtained by fitting to data from DFT.

To analyze the electron-phonon coupling, we rescale the hopping matrix elements in the distorted structures according to Eq. (B1). With the neighbor index n of all quantities understood,

$$\frac{\partial t}{\partial \boldsymbol{a}} = \frac{\partial t}{\partial r}\frac{\partial r}{\partial \boldsymbol{a}} + \frac{\partial t}{\partial \varphi}\frac{\partial \varphi}{\partial \boldsymbol{a}}$$

$$= \frac{\lambda t}{r}\frac{\boldsymbol{a}}{r} + \left[\frac{\partial R_\varphi}{\partial \varphi}R_{-\varphi}t + tR_\varphi\frac{\partial R_{-\varphi}}{\partial \varphi}\right]\frac{R_{\frac{\pi}{2}}\boldsymbol{a}}{r^2}. \tag{B3}$$

Starting from the Hamiltonian in Eq. (5), it is straightforward to derive the formula for the electron-phonon coupling in the orbital basis [cf. Eq. (2.29) of Ref. [80]],

$$g_{q\nu k} = \frac{1}{\sqrt{2\omega_{q\nu}M}}\sum_n \frac{\partial t_n}{\partial \boldsymbol{a}_n}(e^{i a_n k} - e^{i a_n(k+q)}) \cdot \boldsymbol{e}_{q\nu}, \tag{B4}$$

where M is the atomic mass. Neglecting the φ derivatives in Eq. (B3) and noting that both $\nabla_k e^{iak} = iae^{iak}$ and $\nabla_a t = \lambda t \boldsymbol{a}/a^2$ are parallel to $\boldsymbol{a}$, we can rewrite the coupling as [cf.

Eq. (A.8) of Ref. [80]]

$$g_{qvk} = \frac{-i\lambda}{a^2\sqrt{2\omega_{qv}M}}(\boldsymbol{v}_k - \boldsymbol{v}_{k+q}) \cdot \boldsymbol{e}_{qv}, \qquad \text{(B5)}$$

where $\boldsymbol{v}_k = \nabla_k H_k$ is the velocity operator in the orbital basis.

APPENDIX C: COMPUTATIONAL PARAMETERS

All DFT and DFPT calculations are carried out using QUANTUM ESPRESSO [102,103]. The modification that is required for cDFPT is described in detail in Ref. [53]. For the transformation of the electron energies and electron-phonon coupling to the Wannier basis, we use WANNIER90 [104] and the EPW code [65,105].

We apply the generalized gradient approximation (GGA) by Perdew, Burke, and Ernzerhof (PBE) [106,107] and use norm-conserving Hartwigsen-Goedecker-Hutter (HGH) [108,109] pseudopotentials at a plane-wave cutoff of 100 Ry. Uniform meshes (including Γ) of 12×12 $\boldsymbol{q}$ and 36×36 $\boldsymbol{k}$ points are combined with a Fermi-Dirac smearing of 5 mRy. For a fixed cell height of 15 Å, minimizing forces and in-plane pressure to below 1 µRy/Bohr and 0.1 kbar yields a lattice constant of 3.39 Å.

On the model level, for the DFPT comparison shown in Figs. 2(b) and 2(c), we use the same meshes and smearings as stated above. For the $\boldsymbol{q}$-dependent results shown in Fig. 4, we use 360×360 $\boldsymbol{q}$ and $\boldsymbol{k}$ points together with a Fermi-Dirac smearing of 1 meV, if not stated otherwise. For the fluctuation diagnostics for selected $\boldsymbol{q}$ points shown in Figs. 3, 5, 8, and 9, we use 5040×5040 $\boldsymbol{k}$ points together with a Fermi-Dirac smearing of 0.07 meV and a Gaussian smearing of 0.7 meV for the Θ and δ functions in Eqs. (4). The Fermi level is not recalculated for each mesh and smearing but kept fixed at the *ab initio* value throughout this work.

APPENDIX D: EFFECT OF SPIN-ORBIT COUPLING

We have so far disregarded the spin splitting of the electronic bands due to spin-orbit coupling (SOC). In the following, we will briefly outline how SOC affects our findings.

We include SOC by modifying the electronic Hamiltonian, where each spin direction is treated separately [110]. In the basis of real harmonics d_{z^2}, $d_{x^2-y^2}$, and d_{xy},

$$H_{el}^{\uparrow,\downarrow} \rightarrow H_{el}^{\uparrow,\downarrow} \pm \begin{bmatrix} 0 & 0 & 0 \\ 0 & 0 & -i \\ 0 & i & 0 \end{bmatrix} \lambda. \qquad \text{(D1)}$$

We choose a SOC strength $\lambda = 174$ meV to reproduce the splitting of the experimental and theoretical bands in Ref. [85].

Figure 9(a) shows the resulting modified electron dispersion [cf. Fig. 1(b)]. Along Γ-M, the d bands remain spin-
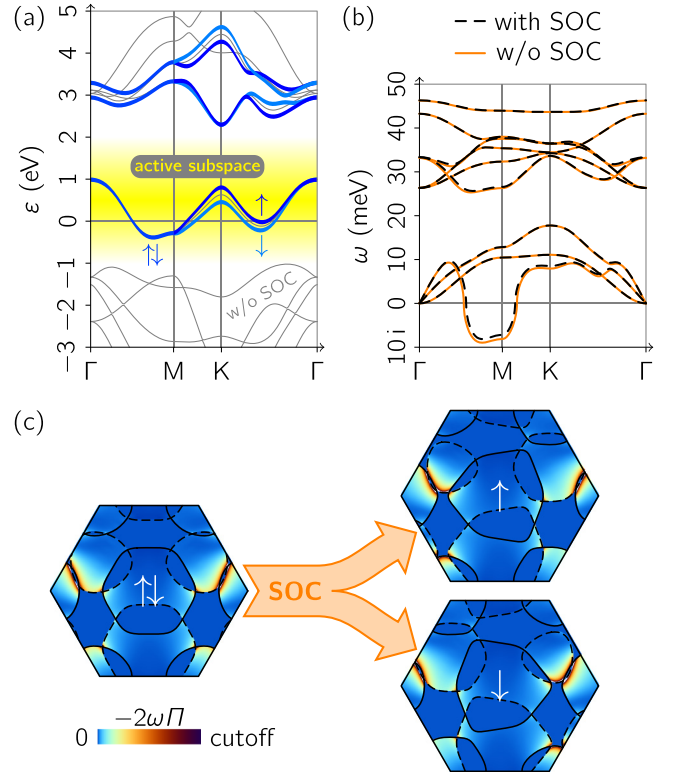

FIG. 9. Effect of SOC on band structures and fluctuations. (a) Spin-resolved electronic band structure. (b) Screened phonon dispersion with and without SOC. (c) Spin- and momentum-resolved LA phonon self-energy for $\boldsymbol{q} = 2/3$ M in the undoped case with (right) and without SOC (left). Solid (dashed) lines indicate the Fermi surface (shifted by $\boldsymbol{q}$) for the respective spin direction(s). To match color scales, the data on the right are multiplied by a factor of 2.

degenerate. Beyond this line, the bands split with a maximum splitting of 2λ of the low-energy band at K.

The screened phonon dispersions with and without SOC according to Eqs. (2) are compared in Fig. 9(b) [cf. Fig. 2(b)]. We note that there is no prefactor of 2 in Eq. (2b) when the spin is explicitly included in the band summations. As expected, SOC does not cause qualitative changes in the phonon dispersion.

This can be explained by the $\boldsymbol{k}$-space fluctuations diagnostics. In Fig. 9(c), the LA phonon self-energy for $\boldsymbol{q} = 2/3$ M in the undoped case is displayed together with the Fermi surface, both with and without SOC [cf. Fig. 3(a)]. The argument of touching K and K′ pockets is hardly affected by SOC: For each spin direction, one pocket shrinks while the other expands, leaving their overlap region and thus the resulting phonon self-energy essentially unchanged.

[1] J. G. Bednorz and K. A. Müller, Possible high-T_c superconductivity in the Ba–La–Cu–O system, Z. Phys. B **64**, 189 (1986).

[2] Z.-X. Shen, A. Lanzara, S. Ishihara, and N. Nagaosa, Role of the electron-phonon interaction in the strongly corre-

lated cuprate superconductors, Philos. Mag. B **82**, 1349 (2002).

[3] O. Gunnarsson and O. Rösch, Interplay between electron–phonon and Coulomb interactions in cuprates, J. Phys.: Condens. Matter **20**, 043201 (2008).

[4] E. Fradkin, S. A. Kivelson, and J. M. Tranquada, Colloquium: Theory of intertwined orders in high temperature superconductors, Rev. Mod. Phys. **87**, 457 (2015).

[5] A. Cavalleri, Photo-induced superconductivity, Contemp. Phys. **59**, 31 (2018).

[6] Y. Kamihara, T. Watanabe, M. Hirano, and H. Hosono, Iron-based layered superconductor La[$O_{1-x}F_x$]FeAs ($x = 0.05$–0.12) with $T_c = 26$ K, J. Am. Chem. Soc. **130**, 3296 (2008).

[7] G. R. Stewart, Superconductivity in iron compounds, Rev. Mod. Phys. **83**, 1589 (2011).

[8] D. Huang and J. E. Hoffman, Monolayer FeSe on $SrTiO_3$, Annu. Rev. Condens. Matter Phys. **8**, 311 (2017).

[9] N. W. Ashcroft, Metallic Hydrogen: A High-Temperature Superconductor? Phys. Rev. Lett. **21**, 1748 (1968).

[10] L. P. Gor'kov and V. Z. Kresin, Colloquium: High pressure and road to room temperature superconductivity, Rev. Mod. Phys. **90**, 011001 (2018).

[11] A. P. Drozdov, P. P. Kong, V. S. Minkov, S. P. Besedin, M. A. Kuzovnikov, S. Mozaffari, L. Balicas, F. F. Balakirev, D. E. Graf, V. B. Prakapenka, E. Greenberg, D. A. Knyazev, M. Tkacz, and M. I. Eremets, Superconductivity at 250 K in lanthanum hydride under high pressures, Nature (London) **569**, 528 (2019).

[12] C. M. Varma and A. L. Simons, Strong-Coupling Theory of Charge-Density-Wave Transitions, Phys. Rev. Lett. **51**, 138 (1983).

[13] J. Wilson, F. Di Salvo, and S. Mahajan, Charge-density waves and superlattices in the metallic layered transition metal dichalcogenides, Adv. Phys. **24**, 117 (1975).

[14] T. M. Rice and G. K. Scott, New Mechanism for a Charge-Density-Wave Instability, Phys. Rev. Lett. **35**, 120 (1975).

[15] R. L. Withers and J. A. Wilson, An examination of the formation and characteristics of charge-density waves in inorganic materials with special reference to the two- and one-dimensional transition-metal chalcogenides, J. Phys. C **19**, 4809 (1986).

[16] K. Rossnagel, On the origin of charge-density waves in select layered transition-metal dichalcogenides, J. Phys.: Condens. Matter **23**, 213001 (2011).

[17] D. Pasquier and O. V. Yazyev, Unified picture of lattice instabilities in metallic transition metal dichalcogenides, Phys. Rev. B **100**, 201103(R) (2019).

[18] A. Cavalleri, T. Dekorsy, H. H. W. Chong, J. C. Kieffer, and R. W. Schoenlein, Evidence for a structurally-driven insulator-to-metal transition in VO_2: A view from the ultrafast timescale, Phys. Rev. B **70**, 161102(R) (2004).

[19] S. Hellmann, T. Rohwer, M. Kalläne, K. Hanff, C. Sohrt, A. Stange, A. Carr, M. M. Murnane, H. C. Kapteyn, L. Kipp, M. Bauer, and K. Rossnagel, Time-domain classification of charge-density-wave insulators, Nat. Commun. **3**, 1 (2012).

[20] L. Perfetti, P. A. Loukakos, M. Lisowski, U. Bovensiepen, H. Berger, S. Biermann, P. S. Cornaglia, A. Georges, and M. Wolf, Time Evolution of the Electronic Structure of 1T-TaS$_2$ Through the Insulator-Metal Transition, Phys. Rev. Lett. **97**, 067402 (2006).

[21] O. Gunnarsson, T. Schäfer, J. P. F. LeBlanc, E. Gull, J. Merino, G. Sangiovanni, G. Rohringer, and A. Toschi, Fluctuation Diagnostics of the Electron Self-Energy: Origin of the Pseudogap Physics, Phys. Rev. Lett. **114**, 236402 (2015).

[22] O. Gunnarsson, T. Schäfer, J. P. F. LeBlanc, J. Merino, G. Sangiovanni, G. Rohringer, and A. Toschi, Parquet decomposition calculations of the electronic self-energy, Phys. Rev. B **93**, 245102 (2016).

[23] J. Wilson and A. Yoffe, The transition metal dichalcogenides: Discussion and interpretation of the observed optical, electrical and structural properties, Adv. Phys. **18**, 193 (1969).

[24] C. Wang, B. Giambattista, C. G. Slough, R. V. Coleman, and M. A. Subramanian, Energy gaps measured by scanning tunneling microscopy, Phys. Rev. B **42**, 8890 (1990).

[25] K. Rossnagel, O. Seifarth, L. Kipp, M. Skibowski, D. Voß, P. Krüger, A. Mazur, and J. Pollmann, Fermi surface of 2H-NbSe$_2$ and its implications on the charge-density-wave mechanism, Phys. Rev. B **64**, 235119 (2001).

[26] T. Valla, A. V. Fedorov, P. D. Johnson, P.-A. Glans, C. McGuinness, K. E. Smith, E. Y. Andrei, and H. Berger, Quasiparticle Spectra, Charge-Density Waves, Superconductivity, and Electron-Phonon Coupling in 2H-NbSe$_2$, Phys. Rev. Lett. **92**, 086401 (2004).

[27] M. D. Johannes, I. I. Mazin, and C. A. Howells, Fermi-surface nesting and the origin of the charge-density wave in NbSe$_2$, Phys. Rev. B **73**, 205102 (2006).

[28] M. Calandra, I. I. Mazin, and F. Mauri, Effect of dimensionality on the charge-density wave in few-layer 2H-NbSe$_2$, Phys. Rev. B **80**, 241108(R) (2009).

[29] F. Weber, S. Rosenkranz, J.-P. Castellan, R. Osborn, R. Hott, R. Heid, K.-P. Bohnen, T. Egami, A. H. Said, and D. Reznik, Extended Phonon Collapse and the Origin of the Charge-Density Wave in 2H-NbSe$_2$, Phys. Rev. Lett. **107**, 107403 (2011).

[30] A. Soumyanarayanan, M. M. Yee, Y. He, J. van Wezel, D. J. Rahn, K. Rossnagel, E. W. Hudson, M. R. Norman, and J. E. Hoffman, Quantum phase transition from triangular to stripe charge order in NbSe$_2$, Proc. Natl. Acad. Sci. (USA) **110**, 1623 (2013).

[31] C. J. Arguello, S. P. Chockalingam, E. P. Rosenthal, L. Zhao, C. Gutiérrez, J. H. Kang, W. C. Chung, R. M. Fernandes, S. Jia, A. J. Millis, R. J. Cava, and A. N. Pasupathy, Visualizing the charge density wave transition in 2H-NbSe$_2$ in real space, Phys. Rev. B **89**, 235115 (2014).

[32] C. J. Arguello, E. P. Rosenthal, E. F. Andrade, W. Jin, P. C. Yeh, N. Zaki, S. Jia, R. J. Cava, R. M. Fernandes, A. J. Millis, T. Valla, R. M. Osgood, and A. N. Pasupathy, Quasiparticle Interference, Quasiparticle Interactions, and the Origin of the Charge Density Wave in 2H-NbSe$_2$, Phys. Rev. Lett. **114**, 037001 (2015).

[33] F. Flicker and J. van Wezel, Charge order from orbital-dependent coupling evidenced by NbSe$_2$, Nat. Commun. **6**, 7034 (2015).

[34] X. Xi, L. Zhao, Z. Wang, H. Berger, L. Forró, J. Shan, and K. F. Mak, Strongly enhanced charge-density-wave order in monolayer NbSe$_2$, Nat. Nanotechnol. **10**, 765 (2015).

[35] X. Zhu, Y. Cao, J. Zhang, E. W. Plummer, and J. Guo, Classification of charge density waves based on their nature, Proc. Natl. Acad. Sci. (USA) **112**, 2367 (2015).

[36] M. M. Ugeda, A. J. Bradley, Y. Zhang, S. Onishi, Y. Chen, W. Ruan, C. Ojeda-Aristizabal, H. Ryu, M. T. Edmonds, H.-Z. Tsai, A. Riss, S.-K. Mo, D. Lee, A. Zettl, Z. Hussain, Z.-X. Shen, and M. F. Crommie, Characterization of

collective ground states in single-layer NbSe$_2$, Nat. Phys. **12**, 92 (2016).

[37] Y. Nakata, K. Sugawara, S. Ichinokura, Y. Okada, T. Hitosugi, T. Koretsune, K. Ueno, S. Hasegawa, T. Takahashi, and T. Sato, Anisotropic band splitting in monolayer NbSe$_2$: Implications for superconductivity and charge density wave, npj 2D Mater. Appl. **2**, 12 (2018).

[38] W. L. McMillan, Microscopic model of charge-density waves in 2H-TaSe$_2$, Phys. Rev. B **16**, 643 (1977).

[39] C. Haas, Chemical bond model of lattice distortions in hexagonal layers, Solid State Commun. **26**, 709 (1978).

[40] J. E. Inglesfield, Bonding and phase transitions in transition metal dichalcogenide layer compounds, J. Phys. C **13**, 17 (1980).

[41] J. E. Inglesfield, Bonding and charge density wave phase transitions, Physica B+C **99**, 238 (1980).

[42] M. H. Whangbo and E. Canadell, Analogies between the concepts of molecular chemistry and solid-state physics concerning structural instabilities. Electronic origin of the structural modulations in layered transition metal dichalcogenides, J. Am. Chem. Soc. **114**, 9587 (1992).

[43] J. A. Silva-Guillén, P. Ordejón, F. Guinea, and E. Canadell, Electronic structure of 2H-NbSe$_2$ single-layers in the CDW state, 2D Mater. **3**, 035028 (2016).

[44] J. A. Wilson, F. J. Di Salvo, and S. Mahajan, Charge-Density Waves in Metallic, Layered, Transition-Metal Dichalcogenides, Phys. Rev. Lett. **32**, 882 (1974).

[45] G. Wexler and A. M. Woolley, Fermi surfaces and band structures of the 2H metallic transition-metal dichalcogenides, J. Phys. C **9**, 1185 (1976).

[46] J. A. Wilson, Charge-density waves in the 2H-TaSe$_2$ family: Action on the Fermi surface, Phys. Rev. B **15**, 5748 (1977).

[47] T. Straub, T. Finteis, R. Claessen, P. Steiner, S. Hüfner, P. Blaha, C. S. Oglesby, and E. Bucher, Charge-Density-Wave Mechanism in 2H-NbSe$_2$: Photoemission Results, Phys. Rev. Lett. **82**, 4504 (1999).

[48] D. W. Shen, Y. Zhang, L. X. Yang, J. Wei, H. W. Ou, J. K. Dong, B. P. Xie, C. He, J. F. Zhao, B. Zhou, M. Arita, K. Shimada, H. Namatame, M. Taniguchi, J. Shi, and D. L. Feng, Primary Role of the Barely Occupied States in the Charge Density Wave Formation of NbSe$_2$, Phys. Rev. Lett. **101**, 226406 (2008).

[49] S. V. Borisenko, A. A. Kordyuk, V. B. Zabolotnyy, D. S. Inosov, D. Evtushinsky, B. Büchner, A. N. Yaresko, A. Varykhalov, R. Follath, W. Eberhardt, L. Patthey, and H. Berger, Two Energy Gaps and Fermi-Surface "Arcs" in NbSe$_2$, Phys. Rev. Lett. **102**, 166402 (2009).

[50] W. C. Tonjes, V. A. Greanya, R. Liu, C. G. Olson, and P. Molinié, Charge-density-wave mechanism in the 2H-NbSe$_2$ family: Angle-resolved photoemission studies, Phys. Rev. B **63**, 235101 (2001).

[51] T. Kiss, T. Yokoya, A. Chainani, S. Shin, T. Hanaguri, M. Nohara, and H. Takagi, Charge-order-maximized momentum-dependent superconductivity, Nat. Phys. **3**, 720 (2007).

[52] F. Aryasetiawan, M. Imada, A. Georges, G. Kotliar, S. Biermann, and A. I. Lichtenstein, Frequency-dependent local interactions and low-energy effective models from electronic structure calculations, Phys. Rev. B **70**, 195104 (2004).

[53] Y. Nomura and R. Arita, Ab initio downfolding for electron-phonon-coupled systems: Constrained density-functional perturbation theory, Phys. Rev. B **92**, 245108 (2015).

[54] S. Baroni, S. de Gironcoli, A. Dal Corso, and P. Giannozzi, Phonons and related crystal properties from density-functional perturbation theory, Rev. Mod. Phys. **73**, 515 (2001).

[55] W. Kohn, Image of the Fermi Surface in the Vibration Spectrum of a Metal, Phys. Rev. Lett. **2**, 393 (1959).

[56] J. P. Tidman, O. Singh, A. E. Curzon, and R. F. Frindt, The phase transition in 2H-TaS$_2$ at 75 K, Philos. Mag. **30**, 1191 (1974).

[57] G. A. Scholz, O. Singh, R. F. Frindt, and A. E. Curzon, Charge density wave commensurability in 2H-TaS$_2$ and Ag$_x$TaS$_2$, Solid State Commun. **44**, 1455 (1982).

[58] R. V. Coleman, B. Giambattista, P. K. Hansma, A. Johnson, W. W. McNairy, and C. G. Slough, Scanning tunnelling microscopy of charge-density waves in transition metal chalcogenides, Adv. Phys. **37**, 559 (1988).

[59] C. Wang, C. G. Slough, and R. V. Coleman, Spectroscopy of dichalcogenides and trichalcogenides using scanning tunneling microscopy, J. Vac. Sci. Technol. B **9**, 1048 (1991).

[60] S. Nagata, T. Aochi, T. Abe, S. Ebisu, T. Hagino, Y. Seki, and K. Tsutsumi, Superconductivity in the layered compound 2H-TaS$_2$, J. Phys. Chem. Solids **53**, 1259 (1992).

[61] H. Lin, W. Huang, K. Zhao, C. Lian, W. Duan, X. Chen, and S.-H. Ji, Growth of atomically thick transition metal sulfide films on graphene/6H-SiC(0001) by molecular beam epitaxy, Nano Res. **11**, 4722 (2018).

[62] J. Hall, N. Ehlen, J. Berges, E. van Loon, C. van Efferen, C. Murray, M. Rösner, J. Li, B. V. Senkovskiy, M. Hell, M. Rolf, T. Heider, M. C. Asensio, J. Avila, L. Plucinski, T. Wehling, A. Grüneis, and T. Michely, Environmental control of charge density wave order in monolayer 2H-TaS$_2$, ACS Nano **13**, 10210 (2019).

[63] Note that in the present formalism, the screened electron-phonon coupling

$$\widetilde{g}_{qvkmn} = \frac{1}{\sqrt{2\omega_{qv}}} \sum_i e_{qiv} \frac{1}{\sqrt{M_i}} \langle \boldsymbol{k}{+}\boldsymbol{q}m | \frac{\widetilde{\partial V}}{\partial u_{qi}} | \boldsymbol{k}n \rangle$$

depends on the screened potential change $\widetilde{\partial V}$ but on the *bare* phonon energies ω and eigenvectors e.

[64] F. Giustino, Electron-phonon interactions from first principles, Rev. Mod. Phys. **89**, 015003 (2017).

[65] F. Giustino, M. L. Cohen, and S. G. Louie, Electron-phonon interaction using Wannier functions, Phys. Rev. B **76**, 165108 (2007).

[66] O. R. Albertini, A. Y. Liu, and M. Calandra, Effect of electron doping on lattice instabilities in single-layer 1H-TaS$_2$, Phys. Rev. B **95**, 235121 (2017).

[67] C. M. Varma and W. Weber, Phonon Dispersion in Transition Metals, Phys. Rev. Lett. **39**, 1094 (1977).

[68] F. Weber, R. Hott, R. Heid, K.-P. Bohnen, S. Rosenkranz, J.-P. Castellan, R. Osborn, A. H. Said, B. M. Leu, and D. Reznik, Optical phonons and the soft mode in 2H-NbSe$_2$, Phys. Rev. B **87**, 245111 (2013).

[69] E. G. Maksimov and S. V. Shulga, Nonadiabatic effects in optical phonon self-energy, Solid State Commun. **97**, 553 (1996).

[70] M. Lazzeri and F. Mauri, Nonadiabatic Kohn Anomaly in a Doped Graphene Monolayer, Phys. Rev. Lett. **97**, 266407 (2006).

[71] N. Caudal, A. M. Saitta, M. Lazzeri, and F. Mauri, Kohn anomalies and nonadiabaticity in doped carbon nanotubes, Phys. Rev. B **75**, 115423 (2007).

[72] S. Pisana, M. Lazzeri, C. Casiraghi, K. S. Novoselov, A. K. Geim, A. C. Ferrari, and F. Mauri, Breakdown of the adiabatic Born-Oppenheimer approximation in graphene, Nat. Mater. **6**, 198 (2007).

[73] S. Piscanec, M. Lazzeri, J. Robertson, A. C. Ferrari, and F. Mauri, Optical phonons in carbon nanotubes: Kohn anomalies, Peierls distortions, and dynamic effects, Phys. Rev. B **75**, 035427 (2007).

[74] A. M. Saitta, M. Lazzeri, M. Calandra, and F. Mauri, Giant Nonadiabatic Effects in Layer Metals: Raman Spectra of Intercalated Graphite Explained, Phys. Rev. Lett. **100**, 226401 (2008).

[75] M. Calandra, G. Profeta, and F. Mauri, Adiabatic and nonadiabatic phonon dispersion in a Wannier function approach, Phys. Rev. B **82**, 165111 (2010).

[76] From the fact that the phonon self-energy $\Pi_{\mu\nu}$ is Hermitian, it follows immediately that the result of Eq. (2b) will not change if we replace $g_\mu^* \tilde{g}_\nu$ by $\tilde{g}_\mu^* g_\nu$ or, as a consequence, the right-hand side of Eq. (3b). All anti-Hermitian parts of the summands in Eq. (2b) cancel.

[77] The information contained in $\partial_\Delta \Pi(\Delta)$ is similar to the information contained in $\text{Im}\Pi(\omega + i0^+)$.

[78] R. E. Peierls, *Quantum Theory of Solids* (Oxford University Press, London, 1955).

[79] L. M. Roth, H. J. Zeiger, and T. A. Kaplan, Generalization of the Ruderman-Kittel-Kasuya-Yosida interaction for nonspherical Fermi surfaces, Phys. Rev. **149**, 519 (1966).

[80] C. M. Varma, E. I. Blount, P. Vashishta, and W. Weber, Electron-phonon interactions in transition metals, Phys. Rev. B **19**, 6130 (1979).

[81] F. J. Di Salvo, J. A. Wilson, B. G. Bagley, and J. V. Waszczak, Effects of doping on charge-density waves in layer compounds, Phys. Rev. B **12**, 2220 (1975).

[82] X. M. Chen, A. J. Miller, C. Nugroho, G. A. de la Peña, Y. I. Joe, A. Kogar, J. D. Brock, J. Geck, G. J. MacDougall, S. L. Cooper, E. Fradkin, D. J. Van Harlingen, and P. Abbamonte, Influence of Ti doping on the incommensurate charge density wave in 1T-TaS₂, Phys. Rev. B **91**, 245113 (2015).

[83] Y. Yu, F. Yang, X. F. Lu, Y. J. Yan, Y.-H. Cho, L. Ma, X. Niu, S. Kim, Y.-W. Son, D. Feng, S. Li, S.-W. Cheong, X. H. Chen, and Y. Zhang, Gate-tunable phase transitions in thin flakes of 1T-TaS₂, Nat. Nanotechnol. **10**, 270 (2015).

[84] D. F. Shao, R. C. Xiao, W. J. Lu, H. Y. Lv, J. Y. Li, X. B. Zhu, and Y. P. Sun, Manipulating charge density waves in 1T-TaS₂ by charge-carrier doping: A first-principles investigation, Phys. Rev. B **94**, 125126 (2016).

[85] C. E. Sanders, M. Dendzik, A. S. Ngankeu, A. Eich, A. Bruix, M. Bianchi, J. A. Miwa, B. Hammer, A. A. Khajetoorians, and P. Hofmann, Crystalline and electronic structure of single-layer TaS₂, Phys. Rev. B **94**, 081404(R) (2016).

[86] B. Shao, A. Eich, C. Sanders, A. S. Ngankeu, M. Bianchi, P. Hofmann, A. A. Khajetoorians, and T. O. Wehling, Pseudodoping of a metallic two-dimensional material by the supporting substrate, Nat. Commun. **10**, 1 (2019).

[87] N. J. Doran, A calculation of the electronic response function in 2H-NbSe₂ including electron-phonon matrix element effects, J. Phys. C **11**, L959 (1978).

[88] A. H. Castro Neto, Charge Density Wave, Superconductivity, and Anomalous Metallic Behavior in 2D Transition Metal Dichalcogenides, Phys. Rev. Lett. **86**, 4382 (2001).

[89] M. D. Johannes and I. I. Mazin, Fermi surface nesting and the origin of charge density waves in metals, Phys. Rev. B **77**, 165135 (2008).

[90] Y. Ge and A. Y. Liu, Effect of dimensionality and spin-orbit coupling on charge-density-wave transition in 2H-TaSe₂, Phys. Rev. B **86**, 104101 (2012).

[91] D. Xiao, G.-B. Liu, W. Feng, X. Xu, and W. Yao, Coupled Spin and Valley Physics in Monolayers of MoS₂ and Other Group-VI Dichalcogenides, Phys. Rev. Lett. **108**, 196802 (2012).

[92] It is instructive to rewrite the valley Hamiltonians and velocity operators in polar coordinates:

$$H_{p\varphi} = v_0 p \boldsymbol{e}_p \cdot \boldsymbol{\sigma}_\tau + \frac{\Delta}{2}\sigma_z,$$
$$\boldsymbol{v}_{p\varphi} = v_0[(\boldsymbol{e}_p \cdot \boldsymbol{\sigma}_\tau)\boldsymbol{e}_p + (\boldsymbol{e}_\varphi \cdot \boldsymbol{\sigma}_\tau)\boldsymbol{e}_\varphi],$$

where $\boldsymbol{\sigma}_\tau = (\tau\sigma_x, \sigma_y)$, $p\,(\varphi)$ is the radial (angular) momentum coordinate, and $\boldsymbol{e}_p\,(\boldsymbol{e}_\varphi)$ are the corresponding unit vectors in the radial (angular) direction. The equal-energy contours are circles with constant p. We see that $\boldsymbol{v}_{p\varphi}$ has contributions perpendicular ($\boldsymbol{e}_p$ direction) and parallel ($\boldsymbol{e}_\varphi$ direction) to the equal-energy contours.

[93] J. A. Wilson, Modelling the contrasting semimetallic characters of TiS₂ and TiSe₂, Phys. Status Solidi B **86**, 11 (1978).

[94] K. Rossnagel, L. Kipp, and M. Skibowski, Charge-density-wave phase transition in 1T-TiSe₂: Excitonic insulator versus band-type Jahn-Teller mechanism, Phys. Rev. B **65**, 235101 (2002).

[95] H. Cercellier, C. Monney, F. Clerc, C. Battaglia, L. Despont, M. G. Garnier, H. Beck, P. Aebi, L. Patthey, H. Berger, and L. Forró, Evidence for an Excitonic Insulator Phase in 1T-TiSe₂, Phys. Rev. Lett. **99**, 146403 (2007).

[96] J. van Wezel, P. Nahai-Williamson, and S. S. Saxena, Exciton-phonon-driven charge density wave in TiSe₂, Phys. Rev. B **81**, 165109 (2010).

[97] C. Monney, C. Battaglia, H. Cercellier, P. Aebi, and H. Beck, Exciton Condensation Driving the Periodic Lattice Distortion of 1T-TiSe₂, Phys. Rev. Lett. **106**, 106404 (2011).

[98] C. Chen, B. Singh, H. Lin, and V. M. Pereira, Reproduction of the Charge Density Wave Phase Diagram in 1T-TiSe₂ Exposes its Excitonic Character, Phys. Rev. Lett. **121**, 226602 (2018).

[99] T. Kaneko, Y. Ohta, and S. Yunoki, Exciton-phonon cooperative mechanism of the triple-q charge-density-wave and antiferroelectric electron polarization in TiSe₂, Phys. Rev. B **97**, 155131 (2018).

[100] D. Pasquier and O. V. Yazyev, Excitonic effects in two-dimensional TiSe₂ from hybrid density functional theory, Phys. Rev. B **98**, 235106 (2018).

[101] W. A. Harrison, *Elementary Electronic Structure*, rev. ed. (World Scientific, Singapore, 2004).

[102] P. Giannozzi, S. Baroni, N. Bonini, M. Calandra, R. Car, C. Cavazzoni, D. Ceresoli, G. L. Chiarotti, M. Cococcioni, I. Dabo, A. D. Corso, S. d. Gironcoli, S. Fabris, G. Fratesi, R. Gebauer, U. Gerstmann, C. Gougoussis, A. Kokalj, M. Lazzeri, L. Martin-Samos, N. Marzari, F. Mauri,

R. Mazzarello, S. Paolini, A. Pasquarello, L. Paulatto, C. Sbraccia, S. Scandolo, G. Sclauzero, A. P. Seitsonen, A. Smogunov, P. Umari, and R. M. Wentzcovitch, QUANTUM ESPRESSO: A modular and open-source software project for quantum simulations of materials, J. Phys.: Condens. Matter **21**, 395502 (2009).

[103] P. Giannozzi, O. Andreussi, T. Brumme, O. Bunau, M. B. Nardelli, M. Calandra, R. Car, C. Cavazzoni, D. Ceresoli, M. Cococcioni, N. Colonna, I. Carnimeo, A. D. Corso, S. d. Gironcoli, P. Delugas, R. A. DiStasio, A. Ferretti, A. Floris, G. Fratesi, G. Fugallo, R. Gebauer, U. Gerstmann, F. Giustino, T. Gorni, J. Jia, M. Kawamura, H.-Y. Ko, A. Kokalj, E. Küçükbenli, M. Lazzeri, M. Marsili, N. Marzari, F. Mauri, N. L. Nguyen, H.-V. Nguyen, A. Otero-de-la-Roza, L. Paulatto, S. Poncé, D. Rocca, R. Sabatini, B. Santra, M. Schlipf, A. P. Seitsonen, A. Smogunov, I. Timrov, T. Thonhauser, P. Umari, N. Vast, X. Wu, and S. Baroni, Advanced capabilities for materials modelling with QUANTUM ESPRESSO, J. Phys.: Condens. Matter **29**, 465901 (2017).

[104] A. A. Mostofi, J. R. Yates, G. Pizzi, Y.-S. Lee, I. Souza, D. Vanderbilt, and N. Marzari, An updated version of WANNIER90: A tool for obtaining maximally-localised Wannier functions, Comput. Phys. Commun. **185**, 2309 (2014).

[105] S. Poncé, E. Margine, C. Verdi, and F. Giustino, EPW: Electron–phonon coupling, transport and superconducting properties using maximally localized Wannier functions, Comput. Phys. Commun. **209**, 116 (2016).

[106] J. P. Perdew, K. Burke, and M. Ernzerhof, Generalized Gradient Approximation Made Simple, Phys. Rev. Lett. **77**, 3865 (1996).

[107] J. P. Perdew, K. Burke, and M. Ernzerhof, Generalized Gradient Approximation Made Simple [Phys. Rev. Lett. 77, 3865 (1996)], Phys. Rev. Lett. **78**, 1396 (1997).

[108] S. Goedecker, M. Teter, and J. Hutter, Separable dual-space Gaussian pseudopotentials, Phys. Rev. B **54**, 1703 (1996).

[109] C. Hartwigsen, S. Goedecker, and J. Hutter, Relativistic separable dual-space Gaussian pseudopotentials from H to Rn, Phys. Rev. B **58**, 3641 (1998).

[110] G.-B. Liu, W.-Y. Shan, Y. Yao, W. Yao, and D. Xiao, Three-band tight-binding model for monolayers of group-VIB transition metal dichalcogenides, Phys. Rev. B **88**, 085433 (2013).